# Modeling Framework for Multiphysics-Multiscale Behavior of Si-C Composite Anode

Xiang Gao[1, 2], Wenquan Lu[3], Jun Xu[1, 2*]

[1]*Department of Mechanical Engineering and Engineering Science, The University of North Carolina at Charlotte, Charlotte, NC 28223, USA*

[2]*Vehicle Energy & Safety Laboratory (VESL), North Carolina Motorsports and Automotive Research Center, The University of North Carolina at Charlotte, Charlotte, NC 28223, USA*

[3] *Chemical Sciences and Engineering Division, Argonne National Laboratory, Argonne, IL 60439, USA*

## Abstract

To achieve the urgent requirement for high energy density in lithium-ion batteries, Si-C composite anode has been spotlighted as one of the most promising alternatives for next-generation batteries. A comprehensive computational model is indispensable in the developing process of the excellent performance of anode material due to the low-realizability, inconvenience, and high-cost of experiments. Herein, a simultaneous multiphysics-multiscale model aiming at the Si-C composite anode was developed. This model was then used to study the effects of Si percentage, mechanical constraint and charging rate in terms of electrochemical and mechanical performances. A better design to achieve high capacity was proposed based on the computational results. Results provide a powerful tool in the design, development, and evaluation of high energy density lithium-ion batteries.

*Correspondence should be sent to Prof. Jun Xu, Email: jun.xu@uncc.edu, Tel: (704)-687-8240, Fax: (704)-687-8240

**Keywords:** Lithium-ion battery; High energy density; Si-C composite anode; Multiphysics and multiscale; Modeling

## Nomenclature

| | | | |
|---|---|---|---|
| $\sigma_r$ | Radius stress of particles | $t_+$ | Li-ion transference number |
| $\sigma_\theta$ | Hoop stress of particles | $\mathbf{J_e}$ | Li-ion flux in the electrolyte |
| G | Shear modulus | $D_e^{eff}$ | Effective Li-ion diffusion coefficient of electrolyte |
| $\lambda$ | Lame constant | $\mathbf{I_s}$ | Current density in solid phase |
| $\Omega_{eff}$ | Effective partial molar volume | $\kappa_s^{eff}$ | The effective electrical conductivity of solid phase |
| $E$ | Elastic modulus | $\Phi_s$ | Potential in solid phase |
| $\upsilon$ | Poisson's ratio | $a_s$ | Effective surface area |
| $\mathbf{F}$ | Deformation gradient | $I$ | Intercalation current density |
| $J_s$ | Li-ion flux | $\varepsilon_e$ | The volume fraction of electrolyte |
| $\Sigma_{ij}$ | Stress component in macroscale | $M$ | Mobility |
| $C_{ijkl}$ | Stiffness tensor in macroscale | $\sigma_h$ | Hydrostatic stress |
| $\Psi_{kl}$ | Strain component in macroscale | $E_{ref}$ | Open circuit potential of the active materials |
| $\mathbf{I_e}$ | Current density in electrolyte | $\kappa_e$ | The electrical conductivity of the electrolyte |
| $\kappa_e^{eff}$ | The effective electrical conductivity of the electrolyte | $\kappa_s$ | The electrical conductivity of the solid phase |
| $\Phi_e$ | Potential in electrolyte | $\varepsilon_s$ | The volume fraction of the solid phase |
| $R$ | Gas constant | $D_e$ | Li-ion diffusion coefficient of electrolyte |
| $T$ | Temperature | $\alpha_a$ | Anode transfer coefficient |
| $F$ | Faraday constant | $\alpha_c$ | Cathode transfer coefficient |
| $f_\pm$ | Electrolyte activity coefficient | $K$ | Rate constant |
| $C_e$ | Li-ion concentration in the electrolyte | $\mu$ | Chemical potential |
| $c$ | Li-ion concentration in particle | $c_{surf}$ | Li-ion concentration in particle surface |

| | |
|---|---|
| $c_{aver}$ | Average Li-ion concentration in particle |

# 1 Introduction

The increasing demand for high-energy-density lithium-ion batteries has attracted a large number of research work on electrode materials[1, 2]. More specifically, alloy-based anode materials, e.g. Si, Ge, and Sn, have become a heated topic among the battery community due to their high theoretical capacities[3, 4]. Despite their high capacity, the biggest disadvantage of such materials is its poor cyclability due to their extra-large volume change (up to 300%) during charging/discharging cycles, which may cause mechanical degradation like particle fragment[5, 6], stress generation[7], as well as the solid-electrolyte interphase (SEI) layer instability[8]. In the past few years, various advanced nanomaterial fabrication strategies, such as nanoparticle[9], nanotube[10, 11], nanowire[12] and thin film[13], have been proposed to mitigate the stress caused by the volume change and highly promising electrochemical performance was obtained. However, the volumetric capacity of electrode fabricated by nanomaterials is low due to the inherent nano-property accompanying low tap density which induces excessive use of binder and conductive agent [14, 15]. Thus, the Si-C composite [16] approach is widely adopted because it has the advantage of nanomaterials as well as compensates the weakness of nano-properties. From these studies, one may see its easier implementation and clear commercialization path compared to the nanomaterials. Currently, Si-C composite anode has been regarded as one of the most promising materials [17-19] to substitute current graphite anode to

achieve higher energy density gradually. Although the lab level fabrication and application of Si-C composite are well developed now [20-22], its large-scale commercialization is still emerging.

In addition to electrochemical characterization, *in-situ,* and microscale experiments, which may give us a better understanding of the new material behaviors, are usually expensive and unavailable[23], not to mention that stress measurement in active particle level is unattainable on such complex structured materials. To alleviate the headache in the experiment methodology, some pioneering theoretical models were proposed. The core components of these models were mainly composed of two parts, i.e. the mechanical model and diffusion model. At the particle level, the mechanical models typically study the elastic behavior[24, 25], consisting of the plastic behavior[26], fracture[27], anisotropic property[28]. The diffusion model is concentration gradient driven, and the stress effects were integrated into the diffusion model[29], considering the coupling effects from the mechanical behavior. At large scale level, Newman model and classical continuum mechanical model were widely used to model the electrochemical and mechanical behaviors of battery cells[30-34]. Furthermore, the coupling strategy of electrochemical and mechanical fields in a large scale were proposed and verified, providing comprehensive knowledge on the multiphysics behavior of battery cells[31, 35-37]. Also, for multiscale electrochemical behaviors, some modeling works have explored the coupling strategy and mechanism, which provide a comprehensive understanding [38-40]. Considering both the mechanical and electrochemical in different scales, a more comprehensive multiphysics

and multiscale model is needed but few studies have been done towards this.

The high capacity battery design requires a multiscale work from material scale to cell scale due to the complex nature of the battery system. It is important to understand the coupling mechanism between material behaviors in microscale and cell behaviors in macroscale during battery development. Some efforts have been made to combine the multiscale as well as the multiphysics in one model by introducing the particles in detail in the electrode of macroscale, which could be very complicated in modeling and computationally expensive [41, 42]. Most recently, a simultaneous multiscale and multiphysics model was reported in which only one kind of active material in the microscale was considered[43, 44].

Compared to pure graphite anode, the Si-C composite brings in extra interfaces between Si and C because the adding of Si is implemented through a Si-C composite particle, as well as nonlinear large deformation across the length-scales. The combined degree of freedom and governing differential equations significantly increase the modeling complexities, hindering the success of model development for multiphysical behaviors of the composite anode.

To bridge the gap, this paper established a modeling framework aiming at Si-C composite anode. Half-cell tests were conducted to capture the electrochemical property of the target material. An *in-situ* full-cell charging/discharging test was conducted to provide the voltage and deformation profiles. A multiphysics-multiscale model for composite anode was then established based on the classical mechanical and pseudo electrochemical model and was validated by the testing data. Based on this

model, two cases with different geometrical configurations to achieve different Si ratios were studied, as well as the constraint effect and charging rate effect. Electrochemical properties such as voltage profile and Li-ion concentration, together with mechanical behaviors such as the stress and deformation will be discussed for all cases to determine a better configuration for high capacity LIB.

## 2 Method

*2.1 Si-C composite anode multiscale characterization*

Without loss of generality, two types of Si-C compound particles with different Si proportions, i.e.20 wt% and 40 wt%, were selected in this study for Case I and Case II, and the physical properties are listed in Table 1. The Si-C compound particles were used to fabricate the composite anode (Fig. 1(a)). The active particle, binder, and conductive agent were mixed with a ratio of 95:1:4 (see Table 1). Then, a classic slurry cast (coating – drying – rolling – assembly) technique was used to get the composite anode. The multiscale structure of Si-C composite anode can be seen in the scanning electron microscope (SEM) images (Figs. 1 (a)-(d)). The active materials of the composite anode (Fig. 1 (a)) is composed of graphite particles (dark part) and Si-C compound particles (bright part), which is fabricated using nano Si particles, graphite particles and amorphous carbon (Fig. 1 (b)). The nano Si particles, graphite particles and amorphous carbon are purchased from BTR New Energy Materials Inc. The cross-sectional SEM images (Fig. 1 (c) and (d)) show that graphite particles (~2 um) serve as skeleton on which the nano Si particles (~100 nm) are attached by adhesive amorphous C in Si-C compound particles, of which the capacity could achieve around 800 mAh/g

and 1200 mAh/g, i.e. more than 2 and 3 times of the theoretical capacity of pure graphite particles, respectively.

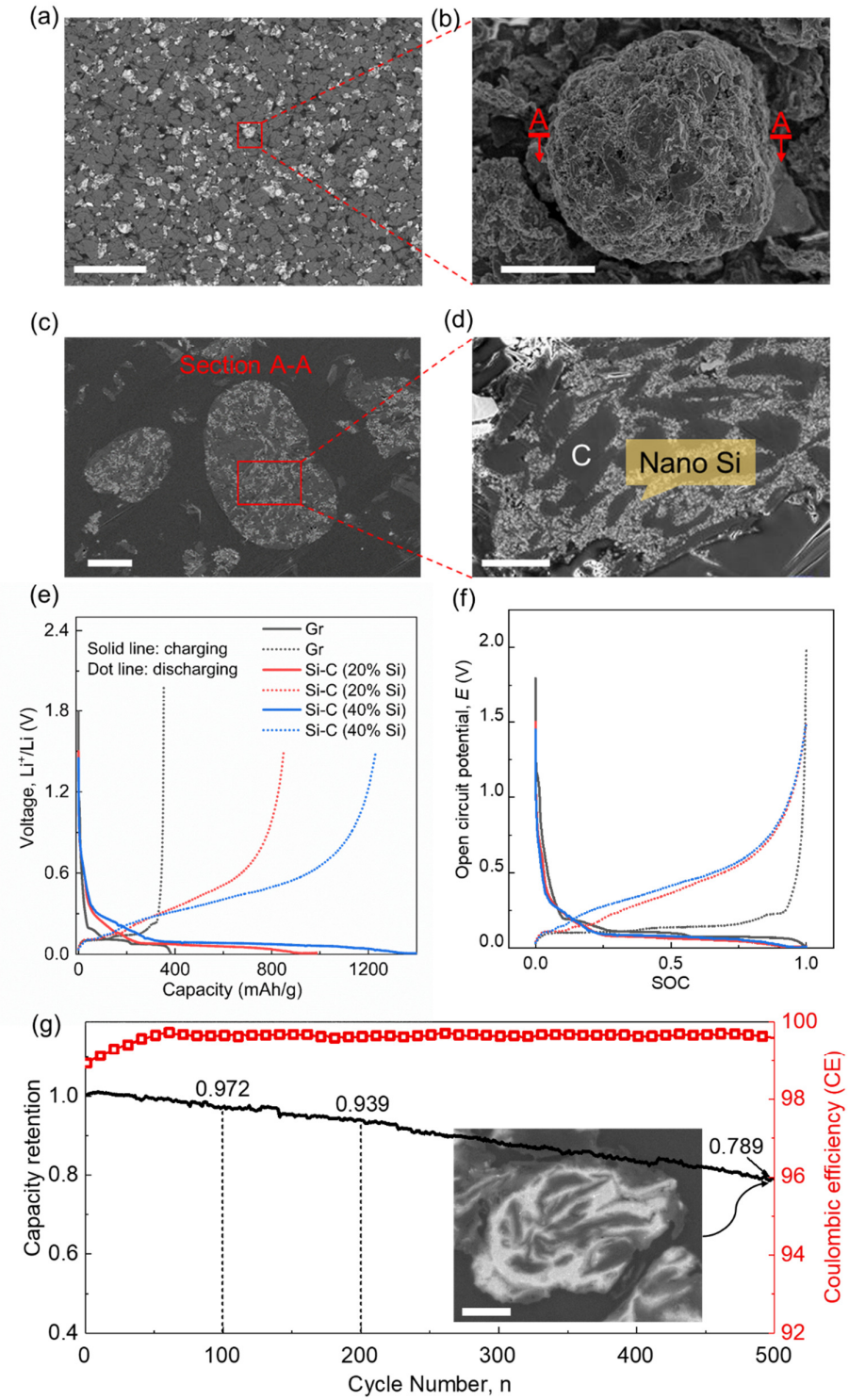


**Fig. 1.** SEM pictures of Si-C composite anode material and the electrochemical characterization.

SEM images of (a) Si-C composite anode (dark zone is C particles and bright particle is Si-C compound particle); (b) Si-C compound particle; (c) cross-section (section A-A) view of Si-C compound particle; (d) nano Si and C particle distribution within Si-C compound particle; (e) half-cell testing for pure graphite anode material and Si-C compound particle material with different Si proportions (20 wt% and 40 wt%); (f) the OCP curves used for modeling corresponding to (e) by change the x-axis to SOC (SOC equals to capacity divided by the corresponding maximum value); (g) Full cell capacity retention at each cycle for $500^{th}$ cycle. The CE is plotted on the secondary y-axis. Inset: SEM images of Si-C compound particle after 500 cycles. Scale bars shown in (a)-(d) and (g) are 5 μm .

Then, the composite anode with 15wt% Si-C compound particles in Case I (the baseline) was used to fabricate half-cell and full-cell for the following tests; the details can be found in Table 2. The cathode used for half-cell is Li metal (purchased from Tianjin Zhongneng) while the $LiCoO_2$ (LCO, purchased from Hunnan Shanshan with a loading of 23.4 mg/cm$^2$) was selected for full-cell. The electrolyte used here was LiPF6 with EC: DMC = 1:1 which was excess, and the excess was squeezed out during package. The final quantity of the electrolyte used in this study was 1.6-1.7g/Ah.

Table 1 Physical properties of two types of Si-C composite anode

| | Si-C comp, wt.% | Si wt.% in Si-C comp | Si wt. % | Graphite, wt.% | Carbon Black, wt.% | Binder, wt.% | Loading, mg/cm$^2$ |
|---|---|---|---|---|---|---|---|
| Case I | 11.25 | 20% | 2.25% | 92.75% | 1% | 4% | \ |
| | 15 | 20% | 3% | 92% | 1% | 4% | 8 |
| | 18.75 | 20% | 3.75% | 91.25% | 1% | 4% | \ |
| Case II | 15 | 20% | 3% | 92% | 1% | 4% | 8 |
| | 15 | 40% | 6% | 89% | 1% | 4% | \ |

Table 2 parameters of half-cell and full-cell used for testing

| | type | Size, mm | Anode thickness, um | Cathode thickness, um | Energy density, Wh/kg |
|---|---|---|---|---|---|
| Half-cell | Coin cell | 13 (radius) | 90-110 | 500 | / |
| Full-cell | One layer | 83*61*0.1 | 44 | 47 | |
| Full-cell | Pouch cell | 73*60*3.88 | 90-110 | 100-120 | 750 |

*2.2 Electrochemical characterization of compound particles*

A half-cell test was constructed on the Si-C composite anode material on the testing system LAND CT2001H. The voltage profiles as a function of the reversible capacities of two types of Si-C compound particles and the pure graphite particles were measured by the constant current and constant voltage techniques with a rate of 0.1C, from 0.005 V to 1.5V (for Si-C compound particles) and 1.8V (for graphite particles). Only the results of the first cycle were measured here. The compound particles with 20% wt Si and 40 wt% Si and the graphite particles exhibited first-cycle gravimetric reversible capacities of 850 mAh/g, 1230 mAh/g and 353 mAh/g, respectively, with initial coulombic efficiencies (CEs) of 86.3%, 86.3% and 92.4%, respectively (Fig. 1 (e)). The curves obtained from the half-cell test are adopted to be the input open circuit potential (OCP) data since the applied current in this test is very tiny. It can be applied as the anode material properties in the following modeling works (Fig. 1(f))

Also, a one-layer full-cell containing one layer of Si-C composite anode, one layer of the separator and one layer of LCO cathode were tested *in situ*. The full-cell configuration was placed in an optical high-power microscope to obtain the real-time deformation video during charging/discharging. At the same time, it was connected to the charging machine and was charged/discharged by the following strategy: CC

charging with a rate of 0.5 C to 4.4V and then convert into CV charging until rate gets down to 0.025C; rest 15 minutes; CC discharging with a rate of 0.5 C to 2.75V; stop. The voltage profiles were recorded. Then the images at different time points were extracted and analyzed to get the deformation values. So, the voltage and deformation were obtained simultaneously in the test and used to validate the computational model.

Cycling tests after the first cycle of the full cell shown in Table 2 were also performed in the voltage range between 2.5V and 4.4 V at 1C on testing system LAND CT2001H. As shown in Fig. 1 (g), the composite anode can keep 97.2% reversible capacity after 100 cycles, 93.9% after 200 cycles and 78.9% after 500 cycles, which is comparable to the current commercial ones. For the CE, it can reach 99.5% after about 37 cycles. This may be explained by the SEM image of Si-C compound particle after 500 cycles that the nano Si exhibited irreversible swelling which may cause severe stress conditions and further lead to fracture and capacity degradation. Thus, the simulation work in the following parts may provide an excellent way to elaborate on the mechanism. Further studies will be conducted in the future besides the multiscale modeling in the current study.

*2.3 Multiphysics-multiscale computational methodology*

The left part of Fig. 2 shows a 3D multiscale structure of the Si-C composite anode (one unit layer with a structure of anode active material-anode current collector-anode active material-separator-cathode active material-cathode current collector-cathode active material). The binder and additives are not considered here and the Si-C compound particles are simplified as a homogenous particle (Supplementary Fig. 1 and

Note 1). To further simplify the modeling process, 2D representative volume element (RVE) model in macroscale (both for mechanical and electrochemical sections) considering only one layer of anode active material, separator and one layer of cathode active material were established where the anode active material was divided into two parts, i.e. C zone and Si-C zone (mid part of Fig. 2). C zone represented the graphite particles which were in dominant quantity while Si-C zone represented the converged Si-C compound particles. Considering the proper simplification (1D simplification in right part of Fig. 2) of the particle shape, several trial simulation works (Supplementary Note 2 and Figs. 2, 3) indicate us to choose four grey circles in 2D model to represent the dispersed Si-C particles by setting the overall weight percentage same as baseline. Then in microscale, single-particle for pure graphite and Si-C particle were simplified into 1D problem and considered by extra dimension node method.

The coupling strategy of field variables is also illustrated in Fig. 2. There are two types of couplings: multiphysics and multiscale. In multiphysics coupling at the microscale level, the average Li-ion concentration ( $c_{aver}$ ) in C particle and Si-C particle increases with charging process (governed by electrochemical model), leading to the swelling behavior of C and Si-C particles (governed by mechanical model). In return, hydrostatic stress ( $\sigma_h$ ) derived from the swelling of two kinds of particles (mechanical model) affects the Li-ion diffusion (electrochemical model). Similarly, the multiphysics coupling at macroscale happens between the average Li-ion concentration ( $c_{aver}$ ) change within C zone and Si-C zone (electrochemical model) and its induced eigen strain ( $\Psi_{ij}$ ) change (mechanical model).

In multiscale coupling of electrochemical model, the intercalation reaction current density ($I$) in macroscale for C zone and Si-C zone that dominates the Li flux on corresponding particle surfaces in microscale would be passed from macroscale to microscale while on the contrary the surface Li-ion concentration ( $c_{surf}$ ) in micro C and Si-C particles that determine the potential of C zone and Si-C zone in macro scale, respectively, would be passed from microscale to macroscale. While in the multiscale coupling of the mechanical model, only the deformation gradient ($F$) would be passed from macroscale to microscale to determine the local deformation. This coupling strategy showed in Fig. 2 can achieve a simultaneously multiphysics-multiscale modeling of the composite anode in single layer Li-ion cells. The principal governing equations are showed in the following sections while the detailed descriptions can be found in Supplementary Note 3.

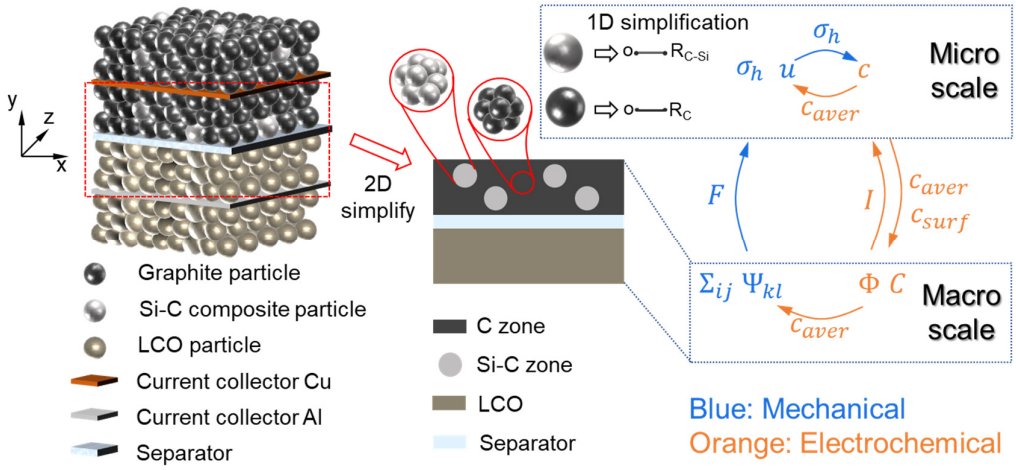


**Fig. 2.** Multiphysics-multiscale modeling methodology with the coupling strategy

2.3.1 Mechanical model in microscale

For spherical particle, the typical equilibrium equation can be described as

$$\frac{\mathrm{d}\sigma_r}{\mathrm{d}r}+\frac{2}{r}\left(\sigma_r-\sigma_\theta\right)=0. \tag{1}$$

In the current study, hydrostatic stress was considered on the surface of particles to represent the effects of surrounding particles, under which the particle would not turn into a plastic stage. Thus, only elastic behaviors are considered here, and the constitutive equation could be derived as

$$\sigma_{ij}=2G\varepsilon_{ij}+\lambda\varepsilon_{kk}\delta_{ij}-\Omega_{eff}\Delta c_s\frac{E}{1-2\upsilon}\delta_{ij}. \tag{2}$$

where $\Delta c_s=c_s-c_s^0$. Different material properties would be applied for C particle and Si-C particle (subscript or superscript "C" and "Si-C" to represent parameters for C particle and Si-C particle, respectively). The boundary conditions could be

$$\begin{aligned} &u_{r,\mathrm{C}}=0 \text{ at } r_{\mathrm{C}}=0\\ &u_{r,\mathrm{Si\text{-}C}}=0 \text{ at } r_{\mathrm{Si\text{-}C}}=0 \end{aligned}, \tag{3}$$

$$\begin{aligned} u_{r,\mathrm{C}}&=\left(\sqrt[3]{\det\mathbf{F}}-1\right)r_{p,\mathrm{C}} \text{ at } r_{\mathrm{C}}=r_{p,\mathrm{C}}\\ u_{r,\mathrm{Si-C}}&=\left(\sqrt[3]{\det\mathbf{F}}-1\right)r_{p,\mathrm{Si-C}} \text{ at } r_{\mathrm{C}}=r_{p,\mathrm{Si-C}} \end{aligned} \tag{4}$$

2.3.2 Electrochemical model in microscale

The composite anode contains two kinds of particles in microscale. Similar to mechanical model in Section 2.3.1, variables like Li-ion concentration, $c_s$, should have two substances that are $c_{s,\mathrm{C}}$ and $c_{s,\mathrm{Si-C}}$. To make the description concise, specific substances are not showed here.

Governing equation of Li-ion diffusion within a particle is[29, 45]

$$\frac{\partial c_s}{\partial t}+\frac{1}{r^2}\frac{\partial r^2J_s}{\partial r}=0. \tag{5}$$

The microscale behaviors are achieved by extra dimension nodes method here. The basic principle is: extra dimension nodes are defined by each macroscale node which

can carry the all the variables from macro electrochemical and mechanical model and is governed by Eq. (5). This method is implemented in COMSOL Multiphysics by weak form equations. Then the weak form of Eq. (5) can be expressed as follows by introducing a test function, $\hat{c}_s$:

$$\int_r \left( \frac{\partial c_s}{\partial t} + \frac{1}{r^2} \frac{\partial r^2 J_s}{\partial r} \right) \hat{c}_s \mathrm{d}r = 0 . \tag{6}$$

The boundary conditions and initial conditions are

$$\frac{\partial c_s}{\partial r} = 0 \text{ at } r = 0 , \tag{7}$$

$$J_s = \frac{I}{F} \text{ at } r = r_p , \tag{8}$$

$$c_s(r) = c_s^0 \text{ at } t = 0 \text{ s} \tag{9}$$

As described before, intercalation reaction current density, *I*, is passed from the macroscale electrochemical model.

2.3.3 Mechanical model in macroscale

The macroscale stress in the composite anode for either C zone or Si-C zone is given by (similarly, substances are not showed here)

$$\Sigma_{ij} = C_{ijkl} (\Psi_{kl} - \Psi_{eigen} \delta_{kl}) \tag{10}$$

The eigen strain of the macroscale materials here, $\Psi_{eigen} \delta_{kl}$, is determined by the volumetric change caused by the Li-ion intercalation/deintercalation of its microscale particles. $\Psi_{eigen}$ is determined by the average Li-ion concentration within the materials, giving

$$\Psi_{eigen} = \frac{\Omega_{eff}}{3} \Delta c_s . \tag{11}$$

The equilibrium of macroscale stress gives

$$\nabla \cdot \boldsymbol{\Sigma}=0 \tag{12}$$

2.3.4 Electrochemical model in macroscale

Porous electrode theory[30] is used to describe the electrochemical behavior of the macroscale. The kinetics of the current density and Li-ion flux density in electrolyte are given by

$$\mathbf{I_e} = -\kappa_e^{eff}\left[\nabla\Phi_e - \frac{2RT}{F}\left(1+\frac{d\ln f_{\pm}}{d\ln C_e}\right)\left(1-t_+\right)\nabla\ln C_e\right], \tag{13}$$

$$\mathbf{J_e} = -D_e^{eff}\nabla C_e + \frac{t_+}{F}\mathbf{I_e}. \tag{14}$$

When it comes to solid phase, the current density is given by

$$\mathbf{I_s} = -\kappa_s^{eff}\nabla\Phi_s. \tag{15}$$

The current density in electrolyte and solid phase can be connected by the intercalation reaction current density, *I*, as described by the following equations:

$$\nabla \cdot \mathbf{I_e} = a_s I, \tag{16}$$

$$\nabla \cdot \mathbf{I_s} = -a_s I, \tag{17}$$

$$\varepsilon_e \frac{\partial C_e}{\partial t} = -\nabla \cdot \mathbf{J_e} + \frac{a_s I}{F}. \tag{18}$$

To make this model more functional and suitable for future aging studies, the formation of the SEI layer is also involved in this computational framework. The following kinetic expression describe the kinetics of the parasitic reaction[46]:

$$i_{SEI} = -(1+HK)\frac{Ji_{ref}}{\exp(\frac{\alpha\eta_{SEI}F}{RT}) + \frac{q_{SEI}fJ}{i_{ref}}} \tag{19}$$

where $i_{ref}$ is the local current density, HK is a dimensionless expansion factor function (which is zero during delithiation), J is the exchange current density for parasitic reaction, $\alpha$ is the transfer coefficient of the electrochemical reduction

reaction, $\eta_{SEI}$ is the overpotential, $q_{SEI} = Fc_{SEI} / A_v$ is the accumulated charge of Li lost related to a concentration of SEI ($c_{SEI}$) and area of particles ($A_v$) and $f$ is a parameter based on the SEI properties. The SEI behavior is mainly dominant in cycling condition so it is not discussed in the present work.

The computational framework mentioned above was then implemented into COMSOL Multiphysics 5.3a platform. A Dell Precision 7820 Tower workstation with 16 CUPs and 3.49 GHz was used.

## 3 Results

To demonstrate the multiphysics-multiscale methodology described in Section 2.3, as mentioned above, a baseline configuration of Case I was established with four circles of Si-C zones of which the Si proportion in corresponding micro Si-C particle is 20 wt% (Fig. 3 (a)). For mechanical boundary conditions, the bottom surface of cathode was fixed while the top surface of the anode was set to be free. Given that the in-plane deformation in anode could be ignored compared with deformation in the thickness direction, symmetrical boundary conditions were applied on both side edges of the RVE model. For electrical boundary conditions, the cathode surface was connected to the ground while a constant current density was applied on the anode surface. The OCP curves used to define the potential of electrodes were from the half-cell test (Fig. 1(e)). All the other parameter values both for the electrochemical model and mechanical model can be found in Table 3. Considering the deformation of cathode (material $LiCoO_2$ (LCO) was used in this study) during cycling are not evident compared to the Si-C composite anode, no multiphysics and multiscale coupling were applied on

cathode. The deformation of the cathode will cause mechanical loading on the anode which may lead to a condition similar to the mechanical constraint boundary. Thus, an analogy can be drawn between the effect of cathode deformation and the effects of mechanical constraint. This model was validated by comparing the results with full-test data.

**Table 3** Input parameters in multphysics-multiscale model

| Parameter | Symbol | Value |
|---|---|---|
| *Microscale* | | |
| Partial molar volume of Si[47] | $\Omega_{Si}$ | $9\times10^{-6}$ $m^3$/mol |
| Partial molar volume of C[48] | $\Omega_C$ | $3.17\times10^{-6}$ $m^3$/mol |
| Modulus of Si[49] | $E_{Si}$ | $E_{Si}(c_{s,Si})$ |
| Modulus of C[48] | $E_C$ | 19.25+82.23$x$ GPa |
| Maximum Li concentration in Si[50] | $c_{s,\max}^{Si}$ | 278000 mol/$m^3$ |
| Maximum Li concentration in C[51] | $c_{s,\max}^{C}$ | 31507 mol/$m^3$ |
| The diffusion coefficient in Si[47] | $D_{Si}$ | $1.67\times10^{-14}$ $m^2$/s |
| The diffusion coefficient in C[52] | $D_C$ | $1\times10^{-9}$ $m^2$/s |
| The radius of Si-C and C | $r_p$ | 5 μm (estimated) |
| *Macroscale* | | |
| Anode thickness | $H_{anode}$ | 44 μm (measured) |
| Cathode thickness | $H_{cathode}$ | 47 μm (measured) |
| Separator thickness | $H_{separator}$ | 9 μm (measured) |
| RVE width of the cell | $W$ | 200 μm (estimated) |
| The volume fraction of solid in electrode | $\varepsilon_s$ | 0.4 (estimated) |
| Volume fraction of electrolyte in electrode | $\varepsilon_e$ | 0.4 (estimated) |
| The electrical conductivity of cathode [53] | $\kappa_s^{cathode}$ | 100 S/m |
| The electrical conductivity of anode [50] | $\kappa_s^{anode}$ | 1 S/m |
| Initial Li-ion concentration in electrolyte [54] | $C_e^0$ | 1000 mol/$m^3$ |
| Diffusion coefficient in electrolyte [51] | $D_e$ | $7.5\times10^{-11}$ $m^2$/s |
| Transference number [54] | $t_+$ | 0.363 |
| Transfer coefficient | $\alpha_a$ $\alpha_c$ | 0.5 (estimated) |

As shown by the comparison of normalized capacity profiles (Fig. 3 (b)),

simulation results well predict the test data within a voltage range of 2.8-4.44V. Average deformations during the charging process for both test and simulation are also compared (Fig. 3 (c)) giving that they are well consistent with each other despite a small deviation of 3%. It also indicates that the volume increase of a Si-C composite anode during charging can reach about 17% which is acceptable for commercial application compared to several reported Si-involved anode materials[18], although it is still a main defect of this kind of materials. The results shown in Fig. 3 (b) and (c) (also see supplementary Movie 1) indicate that the computational model established in this study can accurately predict the electrochemical-mechanical coupling behavior of Li-ion battery cell containing Si-C composite anode and can be used for parametric studies.

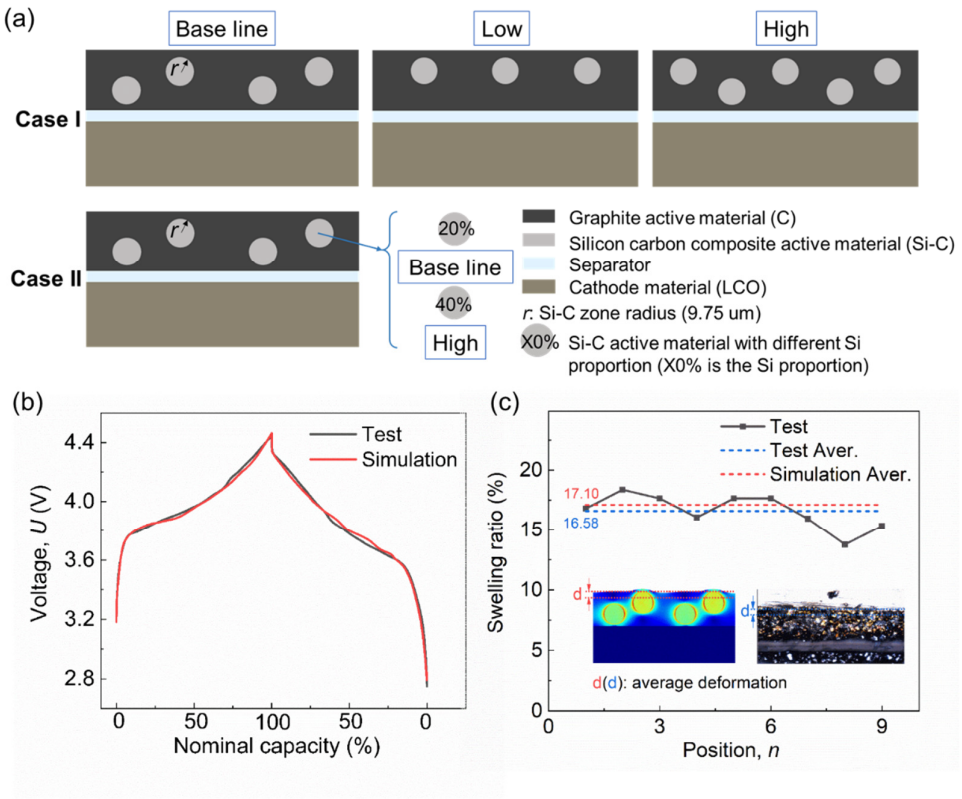


**Fig. 3.** Model configuration and validation. (a) parametric study outline for Case I (different wt% of Si-C compound particle with same Si proportion) and Case II (same wt% of Si-C

compound particles with different Si proportions); (b) and (c) model validation (Case I baseline) in respect to voltage and mechanical deformation, respectively.

## 4 Discussion

To further understand composite anode multiphysics-multiscale mechanism and explore a better configuration aiming for application, a series of parametric studies using this validated model was carried out and analyzed in the following sections.

Basically, there are two types of Cases (Fig. 3(a) and Table 1). Case I and II consider different Si percentages in two different ways: Case I-- different amounts of Si-C zones with same Si proportion in micro particles (20 wt%) are set in anode which gives around 3 wt%, 2.25 wt% and 3.75 wt% overall Si percentages for baseline, Low and High case, respectively; Case II-- same amount of Si-C zones with different Si proportions in microparticles of 20 wt% and 40 wt% are set in anode which give around 3 wt% and 6 wt% overall Si percentages for Baseline and High case, respectively. Besides the Si percentage, constraint effect and charging rate effect are also considered in this study. Except for the parameters described above, all the other settings are the same, including initial conditions and boundary conditions.

### *4.1 Electrochemical behavior for Case I and Case II with and without constraint*

Although the Si proportion was changed for different cases, the thickness of anode and cathode are kept unchanged and the same current density value (10 $A/m^2$ which leads to 0.5C for baseline) was applied for all cases in this part. As shown by the charging and discharging profiles of all cases (Fig. 4 (a) and Supplementary Fig. 4), a

very small difference can be seen in the charging process both for Case I and Case II. However, an obvious difference can be seen from the discharging process for Case II where cell with 40 wt% Si shows a faster voltage drop. This lower voltage profile of the full cell with 40 wt.% Si is due to the higher discharge voltage (delithiation) of the Si-C electrode as shown in Fig. 1 (f). Also, the Li-ion concentration profiles (Fig. 4 (b)) can provide a better understanding of this. A similar tendency can be seen in Fig. 4 (b) among different cases that Li-ion concentration in C zone increases smoothly until reaches its maximum value, while Li-ion concentration in Si-C zones increase faster initially and slow down to a platform, then sharply increase towards its maximum value at the end of charging process. During the discharging process, Li-ion concentration in C zone decreases continuously till it reaches zero at 4000 seconds (about 2/3$^{rd}$ of discharge). On the other hand, Li-ion concentration in the Si-C zone keeps almost unchanged at the beginning and starts to decrease when Li-ion concentration in the C zone is almost zero. Such computational results have good qualitative consistency with the experimental results[55], which can be explained by the different behaviors of C and Si under different potential windows (Fig. 1 (e) and (f)).

Then, by comparing three cases in Case I, one may find that composite anode with a lower percentage of Si-C particles has a higher increasing rate of concentration in the Si-C zone near the end of the charging process. It should be attributed to the fact that the same applied current density would generate the same total amount of transferring Li-ion between anode and cathode. At the beginning of the charging process, the majority of Li-ions are stored mainly within the C zone, little difference is observed in

the Si-C zone. However, when the C zone is almost fully filled, the Si-C zone becomes the dominating material. To store the same total amount of Li-ion, the one with a small amount of Si-C zones need to store more Li-ion in Si-C zones at the same time. This can also explain the discharging behavior among these three cases in Case I that Li-ion concentration in the Si-C zone with less amount of Si-C particles would decrease later. However, for Case II, the mechanism is different due to the various OCP properties of different Si-C compound particles. It is indicated from Fig. 1 (f) that higher Si proportion in Si-C compound particles would make the potential higher at the same SOC value especially for discharging. Fig. 4 (b) shows that more Si addition in Si-C particles significantly increases the Li-ion concentration in the Si-C zone and slightly decrease it in C zone. This can be explained by Fig. 4 (c) which is the overall equilibrium potential of C zone and Si-C zone. It indicates that the equilibrium potential in different materials should keep almost same at the same time, which means C and Si-C materials should be in the same SOC at the same time in the charging process since the charging OCPs are almost the same. Consequently, the Li-ion concentration in the Si-C zone with higher Si proportion increases faster to reach the same SOC since its maximum Li-ion concentration is higher.

On the contrary, Li-ion concentration in C zone would increase slower compared to the baseline to ensure the total Li-ion amount keeps the same simultaneously. These two factors coupled together to determine the Li-ion concentration evolution. For the discharging process, although Si-C zone with lower Si proportion should reach a low SOC faster (Fig. 1 (f)), Li-ion concentration in the one with higher Si proportion

decrease faster instead due to its higher maximum Li-ion concentration value.

The constraint effect is also studied here. A fixed boundary condition was applied on the top surface of the anode considering that different layers would cause constrain effect on each other in the real-world applications of batteries. Fig. 4 (a) and (b) show that constrains on the anode surface does little effect on voltage and Li-ion concentration. The way that mechanical constraint would affect the electrochemical properties is that the constrain can influence the mechanical stress which conversely affects the Li-ion diffusion in the active particles. The results show that the stress plays a minor role in Li-ion diffusion compared to concentration gradient and electrochemical conditions. So the mechanical constraint effect on electrochemical can be ignored. Note that this study only focuses on the first cycle of the battery, when it comes to cycling properties in which the mechanical failure and fatigue behaviors dominate the battery performance degradation, stress effect would be more significant.

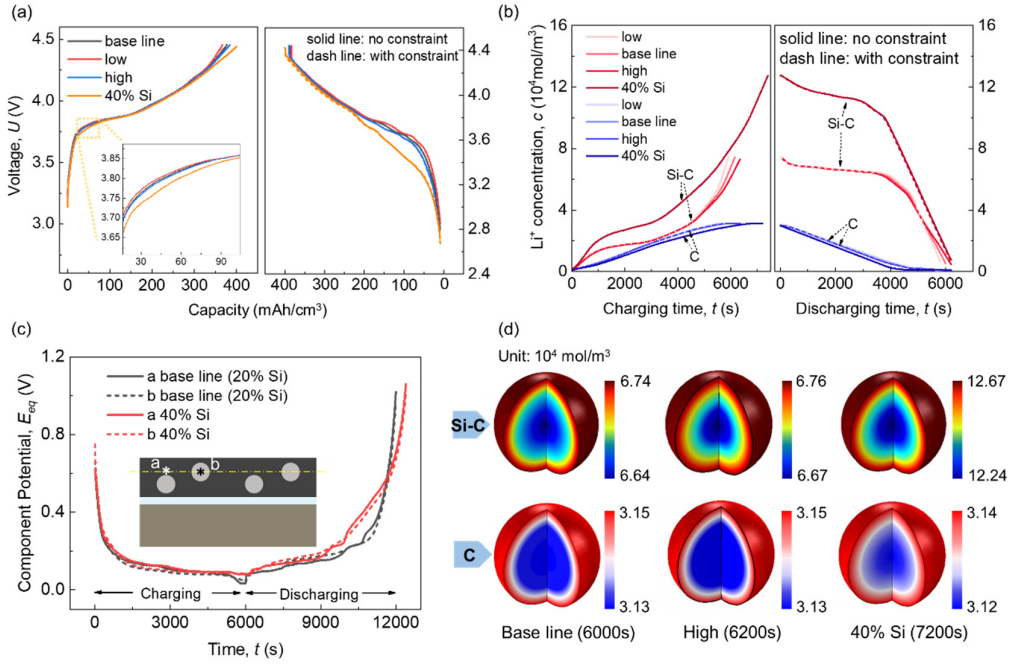

**Fig. 4.** Electrochemical properties for different configurations of Case I and Case II, with and without constraint. (a) voltage comparison; (b) Li concentration comparison in Si-C zone and C zone, respectively, in macro-scale; (c) equilibrium potential in Si-C zone and C zone in macro-scale; (d) Li concentration in Si-C compound particle and C particle in microscale

Furthermore, the Li-ion concentration distributions within microparticle (Si-C compound particle for Si-C zone and C particle from C zone) are analyzed, as shown in Fig. 4 (d). It indicates that the Li-ion concentration gradient along the particle radius is small for all cases since the low charging rate usually leads to a quasi-equilibrium status. The mean value of Li-ion concentration in microscale matches the one in macroscale (Fig. 4 (b)) which indicates that the multiscale model works well.

*4.2 Mechanical behavior for Case I and Case II with and without constraint*

The deformation of the anode is mainly generated by the Si-C zones, which contains nano Si particles (exhibition a maximum of 400% volume change during cycling). From an overall view of Fig. 5 (a), the shapes of curves are very similar to the Li-ion concentration curve (Fig. 4 (b)), which agrees to the conclusion that deformation of Si-C zone is mainly dominated by the Li-ion concentration (electrochemical behavior) and the swelling coefficient (material property).

For Case I, Si-C zones are made of Si-C particles with the same Si proportion in microscale which means they have the same swelling coefficient. From Fig. 4 (b) we know that the Li-ion concentration in Si-C zones has little difference till the end of charging. However, we observe that both the maximum deformation and the average deformation of the anode would be larger with more Si-C zones. It is reasonable that

even the deformation of every single Si-C zone is almost the same, more amount of Si-C could generate more deformation in total. Note that the maximum deformation mostly depends on one single Si-C zone, especially the one closed to the surface, but when the amount of Si-C zone increases, they would affect each other that in-plane deformation is restricted and leading to a larger deformation in the thickness direction. The increase of Si-C zones influences more on average deformation that the overall deformed areas would increase (more green and yellow zones show in the one with more Si-C zones (Fig. 5 (b)).

For Case II, the maximum deformation of the one with 40 wt% Si in Si-C particles shows an extremely huge increase compared with the baseline (20 wt% Si in Si-C particles). This is due to the increased swelling coefficient of the Si-C zone caused by the increased percentage of Si. However, the increase in average deformation is not as huge as that of the maximum deformation. This can be attributed to the fact that the average deformation is a coordinate result from the deformation of the Si-C zone and the constraint of C zone. Thus, to reduce the deformation, deformable zones (or particles in reality) should be embedded as deep as possible into the matrix so that the matrix may help to constrain the deformation. Note that when a fixed boundary condition is applied on the top surface, there will be no deformation of the anode such that the constraint effect on the overall anode deformation is not discussed here.

To analyze the stress within composite anode in macroscale during the charging/discharging behavior, two stress components are considered here, i.e. $\sigma_x$ and $\sigma_y$, in the in-plane and thickness direction, respectively. Two specific points, *a* and *b*,

in two directions were analyzed in this study (Fig. 5 (c)). For both directions, stress component at Point *a* is usually tensile stress while stress at Point *b* is compressive stress. From an overall view, we can see that the stress evolution in both directions behave very similarly as the Li-ion concentration does (Fig. 5 (d) and (e)). This is because the stress here is mainly caused by the deformation of Si-C zones which is directly related to the Li-ion concentration. Due to the Li-ion concentration evolution behavior, the stress in the discharging process would keep the value at the beginning for a while until the Li-ion concentration in the Si-C zone starts to decrease. The tensile stress at Point *a* is the driving force of fracture which may cause cracks in C zone. Compressive stress at Point *b* is one of the responsible reasons for interface crack or debonding between C zone and Si-C zone. This is because if we consider the plastic behavior of C zone which may cause irreversible deformation, the compressive stress here may change into tensile stress which is the driving force of debonding. That means a long platform of stress in discharging would be very harmful. Therefore, a tradeoff between the high capacity (high Si proportion) and mechanical robustness needs to be considered. When considering the constraint effects, the stress evolution changing can be seen in Figs. (d) and (e). A general changing for all cases is that the constraint may contribute to more compressive stress. Thus, stress at Point *b* exhibiting an obvious increase of magnitude while stress at Point *a* decrease. That means the constraint may mitigate the risk of tensile crack in C zone but increase the possibility of debonding and crack at interface of C zone and Si-C zone.

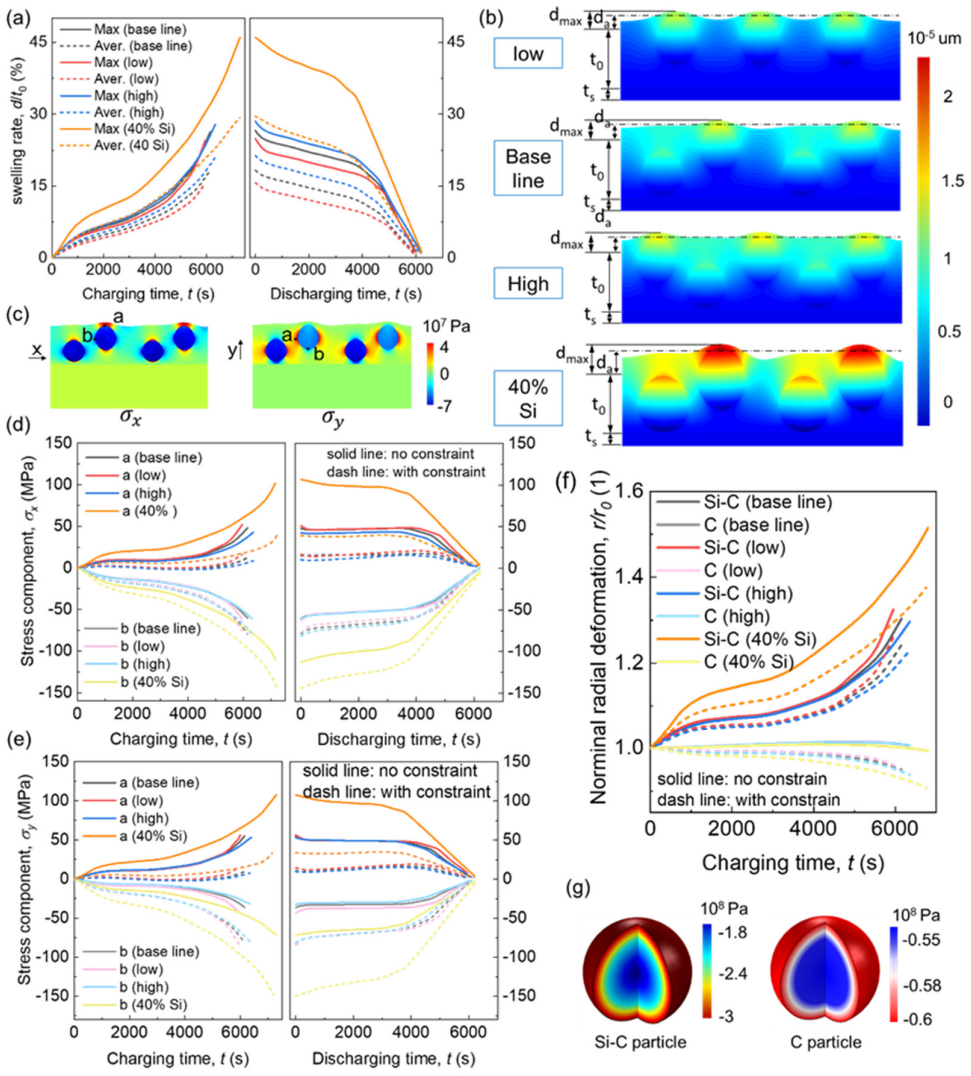


**Fig. 5.** Mechanical properties comparison for different configurations of Case I and Case II, with and without constraint. (a)deformation comparison in macro-scale for Case I and Case II without constraint; (b) deformation distribution in macro-scale for Case I and Case II without constraint; (c) stress extract point and stress component distribution illustration; (d) and (e) stress component along thickness and in-plane direction at two specific points of Si-C zone and C zone in macro-scale; (f) particle radius changes in microscale during charging process for Case I and Case II, with and without constraint; (g) stress distribution in microparticles of baseline.

In microscale, particle radius change shows a similarly trend to the macro deformation (Fig. 5 (f)). Si-C particle shows bigger radius change with a lower amount of Si-C zone for Case I. This is because the Li-ion concentration increase faster in the Si-C zone when the amount of Si-C zone is lower (Fig. 4 (b)). However, when the Si-C particle contains more Si (Case II), the radius shows an obvious increase compared with the baseline. As for the C particles, the radius almost keeps unchanged since the swelling of C can be ignored compared with Si. When considering the constrains, the radius increase of Si-C particles is reduced for all cases. And the radius of C particle shows a decreasing behavior, which is attributed to the extruding caused by the expanding Si-C particles. That means the macroscale constraint boundary condition would have effects on the microscale particle deformation. The deformation behavior of the Si-C and C particles is not only dominated by the Li-ion concentration but also affected by the mechanical boundaries. For the stress in microscale, the baseline case is selected to be the representative (Fig. 5 (g)). The hydrostatic stress at the end of charging in the Si-C particle is larger than that in C particle, and both are in the compressive status. The stress magnitude in microscale particles is slightly larger than that in macroscale due to the porous structure of the anode.

*4.3 Better strategy to achieve high capacity*

In this study, we proposed two ways to achieve the high capacity of composite anode, i.e. Case I and Case II mentioned above. Electromechanical and mechanical properties of all cases from Case I and Case II are discussed in Sections 4.1 and 4.2. To point out which one is a better way to achieve high capacity aiming at commercial

application, a new configuration of Case I called “ultrahigh” with eight Si-C zones was established to achieve a same overall cell capacity with the high-case of Case II (the one with 40 wt% Si in Si-C zone). Considering that the constraint condition is closer to the real working circumstance of batteries, only the models with constraint are studied in this section.

Both electrochemical and mechanical performances are shown in Fig. 6. The voltage profile shows that the voltage of a cell is greatly related to the overall capacity (or Si proportion) rather than the specific structure (Fig. 6 (a) and Supplementary Fig. 5). The Li-ion concentration in Si-C zones of high-case of Case II is much higher than the ultrahigh-case of Case I while the Li-ion concentration in C zones shows little difference (Fig. 6 (b)). The higher Li-ion concentration in the Si-C zone of the high-case of Case II results in a larger deformation of Si-C zones which then leads to larger stress components both in in-plane or thickness direction (Fig. 6 (c) and (d)). As shown in Fig. 6 (e), the Mises stress distribution in macroscale for these two cases further agrees that the overall stress magnitude of the high-case of Case II is larger than that in ultrahigh case of Case I and the large stress usually occurs at the boundary of Si-C zones. The stress in microscale Si-C particles shows that the stress magnitude in Si-C particle from high-case of Case II is almost double to that of the ultrahigh case of Case I. However, the stress in microscale C particles shows an opposite result, which implies that the increase of Si-C zones would play a more important role on C zones.

When achieving the same overall cell capacity, the structure construction as in Case I would generate less deformation and stress in the Si-C zones but the increasing

amounts of Si-C zones would bring more effects on C zone. Considering that the mechanical damage of this kind of composite anode mainly occur within the vicinity of Si-C zones, Case I is a better way to achieve high capacity. Further study needs to be done to obtain the optimal configuration.

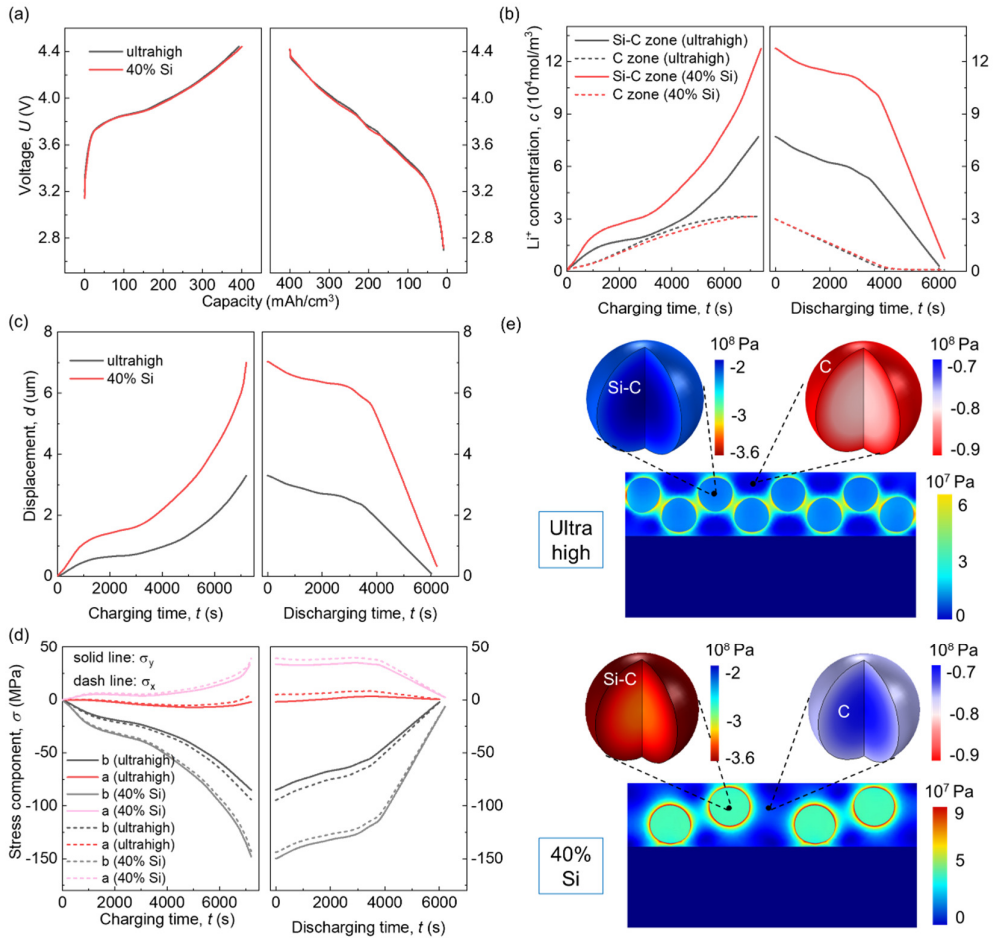


**Fig. 6**. Electrochemical and mechanical properties for ultrahigh case of Case I and the high case of Case II which have the same overall Si ratio in composite anode. (a) voltage comparison; (b) Li concentration comparison in macro-scale; (c) comparison of deformation of Si-C zone; (d) stress component comparison in micro-scale extracted from the same position defined by Fig. 5 (c); (e) stress distribution in different particles in microscale for both cases.

*4.4 Charging rate effects*

To analyze the charging rate effects on this battery cell with the composite anode, two more cases with different current densities of 50 A/m$^2$ and 80 A/m$^2$ are studied based on the baseline case. All the other settings are the same to the baseline discussed in previous sections with constraint. The charging profiles show that a higher charging rate would generate a higher voltage at same SOC so that it would reach the limit voltage at an early SOC (Fig. 7 (a)). It indicates that when the battery cell is charged at a high charging rate, the usable capacity would be reduced. In the meantime, the discharging profiles indicate that a larger voltage drop would occur at the beginning for a higher discharging rate case which may cause a lower discharging platform as well as a lower discharging capacity. This observation agrees well with the Ref.[56]. As shown in Fig. 7 (b), the average Li-ion concentration profiles indicate that the Li-ion concentration increases faster at a higher charging rate in Si-C zones in the charging process while it decreases faster as well in the discharging process.

On the contrary, the Li-ion concentration increases slower at a higher charging rate in C zones in charging process and decrease slower as well in discharging process. The low average Li-ion concentration at the charging end of a high charging rate also implies a low capacity. The Li-ion concentration behavior almost directly dominates the deformation and stress evolution of the Si-C zone (Fig. 7 (c) and (d)). Here, we only discussed the charging process that a higher charging rate would generate a larger deformation of Si-C zone as well as larger stresses during the process. But the final deformation and stresses of the higher charging rate at the charging end are smaller

instead. Then at the discharging process, the initial residual deformation and stresses would be lower for a higher charging rate. Thus, from the mechanical point of view, fast charging is beneficial for the mechanical integrity under the promise of the same nominal voltage at the cost of less utilized capacity though. This can be further explained by the Li-ion concentration profile in microscale particles (Fig. 7 (e)). It indicates that the concentration difference between the particle surface and center would be larger of the higher charging rate, especially for the C particles. Thus, the Li-ion concentration on particle surface which dominates the cell voltage would reach the limit value faster at higher charging rate. Then the average Li-ion concentration would be lower correspondingly, which further causes the lower deformation and stress. It also indicates that the charging rate mainly influences the C materials. Note that the charging rates here are primarily high rates; the slow rates are not considered here. Systematic work describing the slow rates (like C/5, C/10, C/25) will be discussed in the future.

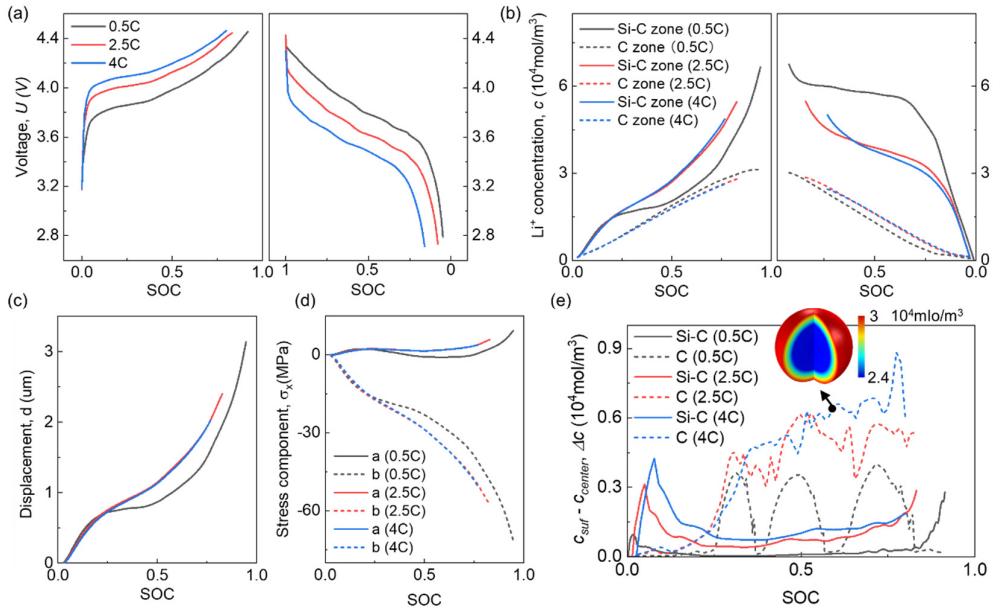

**Fig. 7.** Electrochemical and mechanical properties comparison for different charging rate based on baseline of Case I (a) voltage comparison; (b) Li concentration comparison in macro-scale; (c) comparison of deformation of Si-C zone; (d) stress component comparison in macro-scale extracted from point a of $\sigma\_x$ defined by Fig. 5 (c); (e) Li-ion concentration gradient in different particles of microscale

## 5 Conclusion

A type of Si-C composite anode material was characterized by SEM method. The electromechanical properties of this material were then measured by half-cell and the voltage and mechanical deformation profiles were obtained via *in-situ* full-cell test. In addition, a cycling test was also performed on a pouch cell based on this anode. To further study the electrochemical-mechanical coupling mechanism in battery cell level and microscale particle level, a simultaneous multiphysics-multiscale model was developed and validated.

This model was then used to study the effects of Si ratio, mechanical constraint and charging rate on electrochemical and mechanical performance. Two cases to achieve different Si ratios were considered and Case I (different amounts of Si-C zones in macroscale anode with same Si proportion in microscale Si-C particles) was demonstrated to be a better solution to achieve high capacity. Mechanical constraint showed more effects on mechanical behaviors which may cause electrochemical degradation when considering the cycling behavior. High charging rate would reduce the capacity but generate low deformation and stress of Si-C zones when the battery is

fully charged.

This paper provides a versatile modeling framework to numerically describe the multiphysics and multiscale behaviors of Si-C composite anode. Results pave the path for next-generation anodes design, aiming at high-energy and commercially feasible Si-C composite anodes.

## Reference


[1] J.W. Choi, D. Aurbach, Nat. Rev. Mater., 1 (2016) 16013.
[2] S. Chae, M. Ko, K. Kim, K. Ahn, J. Cho, Joule, 1 (2017) 47-60.
[3] J. Lu, Z. Chen, Z. Ma, F. Pan, L.A. Curtiss, K. Amine, Nat. Nanotechnol., 11 (2016) 1031.
[4] M.T. McDowell, S.W. Lee, W.D. Nix, Y. Cui, Adv. Mater., 25 (2013) 4966-4985.
[5] C.V. Di Leo, E. Rejovitzky, L. Anand, Int. J. Solids Struct., 67-68 (2015) 283-296.
[6] X. Wang, F. Fan, J. Wang, H. Wang, S. Tao, A. Yang, Y. Liu, H. Beng Chew, S.X. Mao, T. Zhu, S. Xia, Nat. Commun., 6 (2015) 8417.
[7] B. Wu, W. Lu, J. Phys. Chem. C, 121 (2017) 19022-19030.
[8] R. Kumar, A. Tokranov, B.W. Sheldon, X. Xiao, Z. Huang, C. Li, T. Mueller, ACS Energy Letters, 1 (2016) 689-697.
[9] Y. Yao, M.T. McDowell, I. Ryu, H. Wu, N. Liu, L. Hu, W.D. Nix, Y. Cui, Nano Lett., 11 (2011) 2949-2954.
[10] M.H. Park, M.G. Kim, J. Joo, K. Kim, J. Kim, S. Ahn, Y. Cui, J. Cho, Nano Lett., 9 (2009) 3844-3847.
[11] H. Wu, G. Chan, J.W. Choi, I. Ryu, Y. Yao, M.T. McDowell, S.W. Lee, A. Jackson, Y. Yang, L. Hu, Y. Cui, Nat. Nanotechnol., 7 (2012) 310.
[12] C.K. Chan, H. Peng, G. Liu, K. McIlwrath, X.F. Zhang, R.A. Huggins, Y. Cui, Nat. Nanotechnol., 3 (2007) 31.
[13] C. Yu, X. Li, T. Ma, J. Rong, R. Zhang, J. Shaffer, Y. An, Q. Liu, B. Wei, H. Jiang, Adv. Energy Mater., 2 (2012) 68-73.
[14] X. Su, Q. Wu, J. Li, X. Xiao, A. Lott, W. Lu, B.W. Sheldon, J. Wu, Adv. Energy Mater., 4 (2014) 1300882.
[15] Y. Jin, B. Zhu, Z. Lu, N. Liu, J. Zhu, Adv. Energy Mater., 7 (2017) 1700715.
[16] X. Wang, Z. Wen, Y. Liu, X. Wu, Electrochim. Acta, 54 (2009) 4662-4667.
[17] Q. Si, K. Hanai, N. Imanishi, M. Kubo, A. Hirano, Y. Takeda, O. Yamamoto, J. Power Sources, 189 (2009) 761-765.
[18] J. Ma, J. Sung, J. Hong, S. Chae, N. Kim, S.-H. Choi, G. Nam, Y. Son, S.Y. Kim, M. Ko, J. Cho, Nat. Commun., 10 (2019) 475.
[19] X. Gao, P. He, J. Ren, J. Xu, Energy Stor. Mater., 18 (2019) 23-33.

[20] M. Ko, S. Chae, J. Ma, N. Kim, H.-W. Lee, Y. Cui, J. Cho, Nat. Energy, 1 (2016) 16113.
[21] Q. Xu, J.-Y. Li, J.-K. Sun, Y.-X. Yin, L.-J. Wan, Y.-G. Guo, Adv. Energy Mater., 7 (2017) 1601481.
[22] L. Gan, H. Guo, Z. Wang, X. Li, W. Peng, J. Wang, S. Huang, M. Su, Electrochimica Acta, 104 (2013) 117-123.
[23] V.A. Sethuraman, A. Nguyen, M.J. Chon, S.P.V. Nadimpalli, H. Wang, D.P. Abraham, A.F. Bower, V.B. Shenoy, P.R. Guduru, J. Electrochem. Soc., 160 (2013) A739-A746.
[24] Y.F. Gao, M. Zhou, J. Appl. Phys., 109 (2011) 014310.
[25] Z. Cui, F. Gao, J. Qu, J. Mech. Phys. Solids, 60 (2012) 1280-1295.
[26] A.F. Bower, P.R. Guduru, V.A. Sethuraman, J. Mech. Phys. Solids, 59 (2011) 804-828.
[27] Y. Qi, Q. Xu, A. Van der Ven, J. Electrochem. Soc., 159 (2012) A1838-A1843.
[28] H. Yang, F. Fan, W. Liang, X. Guo, T. Zhu, S. Zhang, J. Mech. Phys. Solids, 70 (2014) 349-361.
[29] T.H. Wan, F. Ciucci, Electro-Chemo-Mechanics of Solids, (2017) pp. 161-189.
[30] M. Doyle, T.F. Fuller, J. Newman, J. Electrochem. Soc., 140 (1993) 1526-1533.
[31] B. Liu, Y. Jia, J. Li, S. Yin, C. Yuan, Z. Hu, L. Wang, Y. Li, J. Xu, J. Mater. Chem. A, 6 (2018) 21475-21484.
[32] L. Wang, S. Yin, C. Zhang, Y. Huan, J. Xu, J. Power Sources, 392 (2018) 265-273.
[33] B. Liu, S. Yin, J. Xu, Appl. Energy, 183 (2016) 278-289.
[34] L. Wang, S. Yin, J. Xu, J. Power Sources, 413 (2019) 284-292.
[35] B. Liu, H. Zhao, H. Yu, J. Li, J. Xu, Electrochimica Acta, 256 (2017) 172-184.
[36] S. Kim, J. Wee, K. Peters, H.-Y.S. Huang, J. Phys. Chem. C, 122 (2018) 5280-5290.
[37] C. Yuan, X. Gao, H.K. Wong, B. Feng, J. Xu, J. Electrochem. Soc., 166 (2019) A1160-A1169.
[38] A.G. Kashkooli, S. Farhad, D.U. Lee, K. Feng, S. Litster, S.K. Babu, L. Zhu, Z. Chen, J. Power Sources, 307 (2016) 496-509.
[39] S. Pannala, J.A. Turner, S. Allu, W.R. Elwasif, S. Kalnaus, S. Simunovic, A. Kumar, J.J. Billings, H. Wang, J. Nanda, J. Appl. Phys., 118 (2015) 072017.
[40] G. Richardson, G. Denuault, C.P. Please, J. Eng. Math., 72 (2012) 41-72.
[41] W. Wu, X. Xiao, M. Wang, X. Huang, J. Electrochem. Soc., 161 (2014) A803-A813.
[42] M. Wang, X. Xiao, X. Huang, J. Power Sources, 348 (2017) 66-79.
[43] B. Liu, X. Wang, H.-S. Chen, S. Chen, H. Yang, J. Xu, H. Jiang, D.-N. Fang, J. Appl. Mech., 86 (2019) 041005-041005-041012.
[44] B. Wu, W. Lu, J. Mech. Phys. Solids, 125 (2019) 89-111.
[45] E. Bohn, T. Eckl, M. Kamlah, R. McMeeking, J. Electrochem. Soc., 160 (2013) A1638-A1652.
[46] H. Ekström, G. Lindbergh, J. Electrochem. Soc. 162 (2015) A1003-A1007.
[47] M. Wang, X. Xiao, X. Huang, J. Power Sources, 307 (2016) 77-85.
[48] Y. Qi, H. Guo, L.G. Hector, A. Timmons, J. Electrochem. Soc., 157 (2010) A558-

A566.
[49] X. Wang, S.S. Singh, T. Ma, C. Lv, N. Chawla, H. Jiang, Chem. Mater., 29 (2017) 5831-5840.
[50] V.A. Sethuraman, V. Srinivasan, J. Newman, J. Electrochem. Soc., 160 (2013) A394-A403.
[51] V. Srinivasan, J. Newman, J. Electrochem. Soc., 151 (2004) A1530-A1538.
[52] M. Park, X. Zhang, M. Chung, G.B. Less, A.M. Sastry, J. Power Sources, 195 (2010) 7904-7929.
[53] I. Cho, J. Choi, K. Kim, M.-H. Ryou, Y.M. Lee, RSC Advances, 5 (2015) 95073-95078.
[54] M. Doyle, J. Newman, A.S. Gozdz, C.N. Schmutz, J.M. Tarascon, J. Electrochem. Soc., 143 (1996) 1890-1903.
[55] K.P.C. Yao, J.S. Okasinski, K. Kalaga, J.D. Almer, D.P. Abraham, Adv. Energy Mater., 9 (2019) 1803380.
[56] B. Kang, G. Ceder, Nature, 458 (2009) 190.